

RSC Advances



This is an *Accepted Manuscript*, which has been through the Royal Society of Chemistry peer review process and has been accepted for publication.

Accepted Manuscripts are published online shortly after acceptance, before technical editing, formatting and proof reading. Using this free service, authors can make their results available to the community, in citable form, before we publish the edited article. This *Accepted Manuscript* will be replaced by the edited, formatted and paginated article as soon as this is available.

You can find more information about *Accepted Manuscripts* in the [Information for Authors](#).

Please note that technical editing may introduce minor changes to the text and/or graphics, which may alter content. The journal's standard [Terms & Conditions](#) and the [Ethical guidelines](#) still apply. In no event shall the Royal Society of Chemistry be held responsible for any errors or omissions in this *Accepted Manuscript* or any consequences arising from the use of any information it contains.

Highly dispersed MnO_x nanoparticles supported on three-dimensionally ordered macroporous carbon: a novel nanocomposite for catalytic reduction of NO_x with NH₃ at low temperature

Xin Gao ^{a, b}, Ling Li ^b, Lihong Song ^{a, b}, Ting Lu ^b, Jiabin Zhao ^b, Zhi Liu ^{a, b, *}

^aInstitute of Chemistry for Functionalized Materials, Faculty of Chemistry and Chemical Engineering, Liaoning Normal University, Dalian 116029, China

^bFaculty of Chemistry and Chemical Engineering, Liaoning Normal University, Dalian, Liaoning 116029, China

*Corresponding author. Tel.: +86 411 82156989; fax: +86 411 82156858.

E-mail address: zhiliu@lnnu.edu.cn

Abstract

In this paper, we report a novel nanocomposite of MnO_x nanoparticles supported by three-dimensionally ordered macroporous carbon (MnO_x/3DOMC) fabricated by means of a simple multi-component infiltration of three-dimensional templates and its use as a catalyst for low-temperature selective catalytic reduction (SCR) of NO_x with NH₃. Several techniques, including scanning electron microscopy, X-ray diffraction, N₂-sorption, transmission electron microscopy, X-ray photoelectron spectroscopy, NH₃ temperature-programmed desorption, and H₂ temperature-programmed reduction, are employed to characterize the MnO_x/3DOMC nanocomposite. The results demonstrate that the MnO_x/3DOMC possesses highly ordered macroporous structure with hierarchical mesopores in the walls of the macroporous skeleton. MnO_x nanoparticles of 2~4 nm are observed to be highly dispersed on the 3DOM carbon scaffold. Compared with the MnO_x/NAC and MnO_x/TiO₂ catalysts prepared by a conventional impregnation method, the MnO_x/3DOMC catalyst exhibits better low-temperature NH₃-SCR activity, stability, and water vapor and/or SO₂ resistance ability. Such material represents a promising exploring direction for enhancing the catalytic performance of metal oxide-based NH₃-SCR catalysts.

Introduction

Nitrogen oxides (NO_x , $x=1$ or 2), which are mainly emitted from fossil fuels combustion and automobiles, are major hazardous gases for air pollution and human health.^{1,2} Ammonia selective catalytic reduction (NH_3 -SCR) of NO_x to N_2 and H_2O has been successfully developed and commercialized as the most effective flue gas cleaning technologies for stationary sources due to its high-efficiency of NO_x conversion. So far, vanadium-based catalysts, which have exhibited high catalytic activity, selectivity, and SO_2 tolerance within the narrow temperature window of 300-400 °C, are widely used commercial ones for the NH_3 -SCR of NO_x .^{3,4} However, the temperature of the flue gas after the desulfurizer and particulate removal device is generally below 200 °C. Therefore, it is highly desirable to design and fabricate new low-temperature catalysts for the NH_3 -SCR of NO_x . Over the past few years, manganese oxides (MnO_x)-based catalysts have been found to be active for the NH_3 -SCR of NO_x .^{5,6} Recent literature results showed that various MnO_x -based catalysts, such as, nano- MnO_x ,^{7,8} MnO_x /mixed-oxides,^{9,10} MnO_x /ZSM-5,¹¹ MnO_x / TiO_2 ,¹²⁻¹⁴ MnO_x / CeO_2 ,¹⁵ MnO_x /activated carbon,¹⁶ MnO_x /carbon nanotubes,^{17,18} *etc*, also presented a high NO_x conversion at low temperature ($\cong 250$ °C) in the NH_3 -SCR reaction. However, enlarging specific surface area of the support, dispersing the catalytically active species as highly as possible, and realizing an optimized utilization of active sites are still challenging for these MnO_x -based catalysts.

Three-dimensionally ordered macroporous (3DOM) materials, with uniform pore

size and well-defined periodic structure, have triggered increasing interests due to their widespread applications in separation, catalysis, energy storage/conversion systems, and solar cells, etc.¹⁹⁻²⁵ Conventionally, the colloidal crystal templating strategy (CCTS) is employed to prepare 3DOM materials.²⁶ Briefly, uniform monodispersed microspheres, such as polymethyl methacrylate (PMMA), polystyrene (PS) or silica spheres, can assemble into ordered three-dimensional array in densified packing. These ordered arrays offer a 3D scaffold in which a variety of precursors can be infiltrated. After subsequent solidification of the precursors and removal of the colloidal microspheres, periodic 3D framework structures can be obtained successfully. However, the single macroporous size distributions and relatively low surface areas are greatly disadvantageous to the efficient application of the 3DOM materials especially when they are used as supports in catalysis field. In order to address the problems, a upgraded dual 'hard-soft' colloidal crystal templating strategy (dual-CCTS) has been recently proposed to prepare hierarchically porous structure 3DOM materials, in which PMMA or PS microspheres were used as the hard template to create macropores and some surfactants or organics were introduced into the precursors as the soft template to form mesopores.²⁷⁻³³ It is widely accepted that the metal-support interaction and active species dispersion are important factors in the determination of catalytic performances for metal-loaded catalysts. And a larger specific surface area of the support permits higher dispersion of the active phase, which consequently leads to promotional catalytic performance.³⁴⁻³⁶ Obviously supports such as hierarchical 3DOM materials not only possess high surface area for

good active species dispersion, but it can also reduce the diffusion resistance and permit facile transport, thus allowing for the efficient mass transport of the reactant and the product molecules. Moreover, desired active species can be directly introduced into the 3DOM solid-state architecture through using the corresponding metal salt solution(s) as precursor(s) to infiltrate the template. Different from the traditional impregnation, deposit or (co-)precipitation, such a 3DOM catalyst would not only yield intimate contact and strong interaction between the active species and the 3DOM support matrix, but it also make the active species highly dispersed in the 3DOM support matrix, which will potentially give rise to superior catalytic performance.

In the present work, we have successfully prepared a $\text{MnO}_x/3\text{DOM}$ carbon nanocomposite ($\text{MnO}_x/3\text{DOMC}$) by means of a simple multi-component (manganous nitrate, phenol-formaldehyde resol, and triblock copolymer F127) infiltration of 3D PMMA templates followed by a direct pyrolysis process. The NH_3 -SCR of NO_x was used as a probe reaction to evaluate the catalytic performance of the $\text{MnO}_x/3\text{DOMC}$. The results showed that the MnO_x nanoparticles prepared with the dual-CCTS were highly dispersed in the 3DOM carbon scaffold, and the new nanocomposite presented a higher catalytic activity than those of the others MnO_x -based catalysts prepared by the conventional impregnation method in the NH_3 -SCR of NO_x .

Experimental

Synthesis of PMMA template

The PMMA colloidal crystal templates were synthesized via a soap-free-emulsion

polymerization according to a modified procedure based on Ref. 37. In a typical synthesis, a required amount of monomer MMA was washed three times with a NaOH solution (10 wt.%) and di-distilled water respectively to remove any traces of the inhibitor. Then, 11.3 g of the washed MMA and 150 g of di-distilled water were added to a 500 mL round bottom flask and stirred for a while. Then, 12 mL (0.0005 g mL^{-1}) $\text{K}_2\text{S}_2\text{O}_8$ was added to the solution and the mixture was constantly reacted at $70 \text{ }^\circ\text{C}$ for 7 h under a nitrogen atmosphere with mild stirring until a milky solution appeared. After filtering the milky solution to remove large agglomerates, the monodispersed PMMA microspheres were obtained. Finally, the as-synthesized monodispersed PMMA microspheres were packed into PMMA colloidal crystal template by evaporating the water solvent at $70 \text{ }^\circ\text{C}$ for 24 h.

Preparation of precursors

The phenol-formaldehyde (P-F) resol precursor was prepared according to Ref. 38. Briefly, 6.0 g of phenol was mixed with 1.0 g of 20 wt.% NaOH aqueous solution under stirring, and 10.0 g of formaldehyde solution was then added. The resulting transparent solution was stirred at $75 \text{ }^\circ\text{C}$ for 1 h, cooled to room temperature, and the pH was then adjusted to about 7.0 by 2.0 mol L^{-1} HCl. After water was removed by distillation, the mixture was redispersed in a required amount of ethanol. The NaCl precipitate was removed by filtration, and the filtrate, the P-F resol precursor with a concentration of 50 wt.% in ethanol, was collected for further use. For a typical synthesis of manganese precursor (MP), 0.23 g of $\text{Mn}(\text{NO}_3)_2$ solution (50 wt.%) was dissolved in 10.0 g of ethanol under stirring for 30min. Next, 1.0 g of P-F resol was

added to the solution and stirred for another 1 h. The above resulting mixture was added into 0.2 g of F127 and then stirred overnight.

Preparation of MnO_x/3DOMC catalyst

The MnO_x/3DOMC was prepared by employing the CCTS with the as-prepared MP. Typically, the PMMA template was firstly soaked in the MP for 30 min. Care was taken to keep the solution level below the top of the PMMA template. After wiping off the excess solution, the infiltrated template was dried at 100 °C for 2 h. Then, the soaking-drying steps were repeated for three times to ensure a complete filling of the void spaces between the PMMA microspheres. Afterwards, the product was pyrolyzed under flowing N₂ at 450 °C for 2 h and then at 800 °C for another 3 h with a heating rate of 1 °C min⁻¹ to remove the PMMA template and carbonize P-F resol. Finally, the desired MnO_x/3DOMC catalyst was obtained. The total loading amount of manganese in the nanocomposite was 7.1 wt.%, which was determined by inductively coupled plasma (ICP) analysis.

For comparison, commercial Norit activated carbon (NAC) and TiO₂ were used as supports for preparing the MnO_x/NAC and MnO_x/TiO₂ catalysts by a conventional impregnation method. Briefly, 0.2 g of NAC or TiO₂ was dispersed in a certain amount of Mn(NO₃)₂ solution (50 wt.%). The mixture was ultrasonicated for 1 h and then dried overnight at 80 °C. Then, the catalysts were calcined under flowing N₂ at 500 °C for 3 h. The total loading amounts of manganese on MnO_x/NAC and MnO_x/TiO₂ were 7.3 wt.% and 7.4 wt.% (ICP analysis), respectively.

Characterizations

Scanning electron microscope (SEM) experiments were performed with a JSM 6360-LV electron microscope. The samples were vapor-deposited with gold before observation. X-ray diffraction (XRD) patterns were collected with a D/Max- β b diffractometer using a Cu K α radiation source ($\lambda=0.15432$ nm). Wide-angle diffractions were recorded at a scanning speed of 5° min^{-1} . X-ray photoelectron spectroscopy (XPS) measurements were conducted using a PHI 5700 ESCA spectrometer with monochromated Al K α radiation ($h\nu = 1486.6$ eV). Spectra correction was conducted using the C 1s line at 284.6 eV. Chemical compositions of the samples were determined by ICP spectrometer (ICP-AES) on an IRIS Intrepid II XSP instrument. Transmission electron microscopy (TEM) images were obtained on a JEOL 2000EX electron microscope operating at an accelerating voltage of 120 kV. Prior to the observation, the samples were ultrasonically dispersed in ethanol and then dropped onto carbon-coated copper grids. Nitrogen adsorption-desorption isotherms were measured at -196°C on a Micromeritics ASAP 2010 apparatus. The specific surface areas of samples were calculated by the Brunauer-Emmett-Teller (BET) equation. The total pore volumes (V_p) were estimated from the adsorption branches at a relative pressure (P/P_0) of 0.995. The mesopore distributions and the mesopore volumes (V_{meso}) were derived from the desorption branches of the isotherms using the BJH method while the micropore volumes (V_{mic}) were obtained by the t -plot method. Temperature-programmed desorption measurements of ammonia (NH_3 -TPD) of the catalysts were performed with a FineSorb 3010p NH_3 -TPD automated catalyst characterization apparatus. 0.10 g of catalyst was loaded in a quartz reactor, pretreated

at 200 °C for 1 h in He flow (20 mL min⁻¹), and cooled down to 100 °C ready for measurement. The adsorption of NH₃ was performed at 100 °C using pulse model. After adsorption saturation, the catalyst was heated linearly with a rate of 10 °C min⁻¹, from 100 to 700 °C under a constant He flow of 30 ml min⁻¹. The desorbed amount of NH₃ was monitored with a thermal conductivity detector (TCD). Diffuse reflectance infrared Fourier transform spectrum (DRIFTS) was measured on a Bruker Tensor 27 Fourier transform infrared spectrometer (FTIR) equipped with a heated and evacuated custom-made reaction cell with CaF₂ windows connected to a gas-dosing and evacuation system. The catalyst was pressed into a self-supporting wafer with a diameter of 20 mm and a weight of 50 mg. Prior to acquisition of the DRIFTS, the catalyst was pretreated at 200 °C for 1 h in He flow (20 mL min⁻¹) to clean the catalyst surface. After cooling to the room temperature and collecting the background spectra, the catalyst was exposed to pyridine steam for 30 min. Then the reaction cell was evacuated to remove weakly physisorbed pyridine, and the DRIFTS was recorded at room temperature with a spectra resolution of 4 cm⁻¹. Temperature-programmed reduction of hydrogen (H₂-TPR) of the catalysts were carried out on an AutoChem II 2910 chemisorber using 5% H₂ diluted with N₂ (50 mL min⁻¹). 0.1 g of catalyst was firstly pretreated under N₂ flow at 200 °C for 1 h. After cooling to room temperature, the catalyst was programmed heated to 700 °C at a ramping rate of 10 °C min⁻¹. The H₂ consumption during the experiment was monitored by a TCD.

Catalytic measurements

The catalytic activities of the catalysts for the NH₃-SCR were carried out in a quartz

tube fixed-bed continuous flow microreactor containing 200 mg of the sieved catalyst (40-60 mesh). The typical feed gas composition was as follows: 1000 ppm of NO, 1000 ppm of NH₃, 5% of O₂, 5% of water vapor (if necessary), 200 ppm of SO₂ (if necessary), and the balance of He. The water vapor was generated by passing He flow through a gas-wash device containing de-ionized water. The total flow rate was 300 ml min⁻¹, which was equivalent to a gas hourly space velocity (GHSV) of 36000 h⁻¹ for the MnO_x/3DOMC and MnO_x/NAC catalysts, and 40000 h⁻¹ for the MnO_x/TiO₂ catalyst (based on their actual volumes). The molar flow rate of the NO in feed gas was 2.23×10^{-7} mol s⁻¹. The concentration of NO in the inlet and outlet gas was measured by a NO_x analyzer (Eco Physics CLD 70S). All of the data were collected after 20 min when the SCR reaction reached a steady state. The NO conversion is calculated from the variation of the detected NO concentration: NO conversion (%) = $(1 - [\text{NO}]_{\text{out}} / [\text{NO}]_{\text{in}}) \times 100$, where [NO]_{in} is the inlet NO concentration and [NO]_{out} is the outlet NO concentration. Preliminary testing showed that the current MnO_x/3DOMC catalyst possessed the most intact-solid 3DOM architecture with a relatively high manganese content and the best NH₃-SCR activity. Decreasing or further increasing the amount of Mn(NO₃)₂ in the MP caused pores blockage and damage of the corresponding product, and thus was disadvantageous to the increase of the NH₃-SCR activity (Fig. S1-S2).

Calculation of turnover frequencies (TOFs)

The TOF, reflecting the conventional calculation of turnover frequency of NO over each manganese atom, is investigated in order to compare the intrinsic activities of the

present MnO_x/3DOMC catalyst with other MnO_x-based catalysts previously reported in the NH₃-SCR of NO_x. Since the active phase of catalyst, MnO_x, is not atomically dispersed on the support, the relative TOF of NO over per Mn atom is defined as the following equation:³⁹

$$TOF = X_{NO}V_{NO} \frac{M}{m_{Cat}X}$$

where X_{NO} is the NO conversion at certain temperature, V_{NO} is the flow rate of NO (mol s⁻¹), m_{Cat} is the amount of catalyst (g), X is the manganese content in the catalyst determined from XPS (wt.%), and M is the molar weight of manganese (54.9 g mol⁻¹).

Results and discussion

Characteristics of MnO_x/3DOMC

Fig. 1a depicts the representative SEM image of the PMMA template. It was seen that the PMMA template was perfectly uniform and orderly with long range in a large area. A face-centered cubic array of microspheres of ~320 nm with different facets could be clearly observed from the fractured surface. Fig. 1b depicts the representative SEM image of the MnO_x/3DOMC catalyst. It was observed that the MnO_x/3DOMC displayed a high-quality 3DOM structure with a small quantity of point defects and line defects. The macropore size and wall thickness of the sample were ~190 nm and ~50 nm, respectively, which corresponded to shrinkage of ~40% compared with the initial size of the PMMA microspheres. In addition, the next layer was highly visible through the defects, and the voids were interconnected through open window.

XRD results of the MnO_x/3DOMC, MnO_x/NAC, and MnO_x/TiO₂ catalysts are compared in Fig. 2. For the MnO_x/3DOMC, only two broad diffraction peaks at 22.5°

and 43.5° characteristic of amorphous carbon appeared,^{40, 41} and no any crystalline phases of MnO_x were observed, suggesting their possible high dispersion in the 3DOM carbon matrices. For the MnO_x/NAC , in addition to the diffraction peaks of amorphous carbon, two diffraction peaks at 43.2° and 50.5° , ascribed to the characteristics diffraction peaks of tetragonal symmetry of $\alpha\text{-MnO}_2$ (JCPDS 44-0141), were observed clearly, indicating the presence of MnO_x with larger particle sizes in this catalyst than in the $\text{MnO}_x/3\text{DOMC}$. In addition, no diffraction peaks for other manganese oxides were detected. For the $\text{MnO}_x/\text{TiO}_2$, the different diffraction peaks, assignable to the anatase TiO_2 (JCPDS 21-1272), MnO_2 (JCPDS 44-0141) and Mn_2O_3 (JCPDS 41-1442), respectively, could be found easily.

Fig. 3 presents the N_2 adsorption-desorption isotherms and pore size distributions (PSDs) of the $\text{MnO}_x/3\text{DOMC}$, MnO_x/NAC , and $\text{MnO}_x/\text{TiO}_2$ catalysts. For the $\text{MnO}_x/3\text{DOMC}$, the isotherm belonged to a mixed type combining macropores with certain meso- and micropores, which exhibited a type II isotherm with an H3-type hysteresis loop and three N_2 uptake phases. Below the very low relative pressure of $P/P_0 = 0.1$, there was a significant quick rise of adsorption branch, indicating the presence of some micropores generated possibly from the carbonization of P-F resol. With the increase of the relative pressure from $P/P_0 = 0.1$ to $P/P_0 = 0.8$, the N_2 adsorption amounts increased gradually accompanying with a slight H2-type hysteresis loop related to the capillary condensation taking place, implying the existence of some mesopores of a variety of sizes. At high relative pressures of $P/P_0 = 0.8-1.0$, an obvious H3-type hysteresis loop, which had no clear adsorption plateau at

$P/P_0 \approx 1.0$, indicative of a macroporous size distribution, was observed. Such a phenomenon was also observed in the others surfactants-assisted preparation of 3DOM materials,⁴²⁻⁴⁹ feature of combination of macro-mesopore structure. The PSD of the $\text{MnO}_x/3\text{DOMC}$, which centered at ~ 5 nm and ~ 60 nm, respectively, also confirmed this point. In comparison with the $\text{MnO}_x/3\text{DOMC}$, the hysteresis loops of the MnO_x/NAC and $\text{MnO}_x/\text{TiO}_2$ at the low and high relative pressure ranges varied from sample to sample, reflecting their discrepancy in PSD with the $\text{MnO}_x/3\text{DOMC}$. For the MnO_x/NAC , three peaks centering at ~ 3.0 , 4.1 , and 6.5 nm were observed in the PSD curve. Moreover, broad peaks between 20-60 nm were also observed, implying the inhomogeneity of its PSD. For the $\text{MnO}_x/\text{TiO}_2$, a wide PSD from 20 to 300 nm with two small bimodal distributions centering at ~ 30 and ~ 110 nm was observed, which possibly originated from the interstitial spaces between agglomerated particles. Table 1 lists the corresponding textural properties of the three catalysts. The MnO_x/NAC possessed a BET surface area of $659 \text{ m}^2 \text{ g}^{-1}$ and a V_p of $0.38 \text{ cm}^3 \text{ g}^{-1}$. Its V_{meso} and V_{mic} were 0.10 and $0.26 \text{ cm}^3 \text{ g}^{-1}$, respectively, indicating that substantial micropores were present and contributed to the major surface area of the catalyst. On the contrary, despite the fact that the $\text{MnO}_x/3\text{DOMC}$ had a similar BET surface area of $656 \text{ m}^2 \text{ g}^{-1}$ to the MnO_x/NAC , the V_{meso} strikingly increased to $0.36 \text{ cm}^3 \text{ g}^{-1}$ accompanying with a distinct decrease of corresponding V_{mic} to $0.04 \text{ cm}^3 \text{ g}^{-1}$, suggesting that the introduction of F127 during the preparation process could substantially increase the mesoporosity, which favored the significant enhancement in surface area of the obtained $\text{MnO}_x/3\text{DOMC}$ catalyst. In addition, the $\text{MnO}_x/\text{TiO}_2$ had

the smallest the BET surface area of $68 \text{ m}^2 \text{ g}^{-1}$ and the pore volume of $0.11 \text{ cm}^3 \text{ g}^{-1}$ among the catalysts

Since the incomplete certain of manganese valence, XPS was adopted to further identify the components, oxidation states of manganese, and corresponding surface atomic concentration information of the $\text{MnO}_x/3\text{DOMC}$, MnO_x/NAC , and $\text{MnO}_x/\text{TiO}_2$ catalysts, as shown in Fig. 4. For the $\text{MnO}_x/3\text{DOMC}$, the binding energies (BEs) of Mn $2p_{3/2}$ and $2p_{1/2}$ located at 642.1 and 653.8 eV, respectively, with a spin-energy separation of 11.7 eV, suggesting that the predominant oxidation state of manganese is $+4$.⁵⁰ For the MnO_x/NAC , the BEs of Mn $2p_{3/2}$ and $2p_{1/2}$ located at about 642.0 and 653.9 eV, respectively, which can be considered to be identical to those of the $\text{MnO}_x/3\text{DOMC}$ with a Mn^{4+} oxide phase. Unlike the $\text{MnO}_x/3\text{DOMC}$ and MnO_x/NAC , the distinctive Mn $2p_{3/2}$ shoulder-peak of the $\text{MnO}_x/\text{TiO}_2$ could be deconvoluted into three characteristic peaks at BEs of 643.4 eV, 642.0 eV, and 640.3 eV, which were attributed to Mn^{4+} , Mn^{3+} , and Mn^{2+} oxide phases, respectively.⁵¹ Table 2 summarizes the surface atomic concentrations of manganese and the relative concentration ratios of Mn^{4+} , calculated from the XPS spectra. The concentration ratio of Mn^{4+} over the $\text{MnO}_x/3\text{DOMC}$, MnO_x/NAC and $\text{MnO}_x/\text{TiO}_2$ catalysts were presented as 96%, 76%, and 49%. According to the total surface manganese concentrations over the catalysts, 1.65 at.% for the $\text{MnO}_x/3\text{DOMC}$, 1.00 at.% for the MnO_x/NAC , and 1.60 at.% for the $\text{MnO}_x/\text{TiO}_2$, the concentrations of Mn^{4+} over the catalysts were calculated to be 1.50 at.%, 0.76 at.% and 0.78 at.%, respectively. Evidently, the molar concentration of Mn^{4+} on the $\text{MnO}_x/3\text{DOMC}$ was much higher

than that on the other two catalysts. Such discrepancy was presumably associated with the difference in catalyst preparation. In our case, the MnO_x/3DOMC catalyst prepared by the dual-CCTS possessed higher manganese precursor (Mn(NO₃)₂) dispersion and exposed more manganese atoms on the surface than the other two catalysts prepared by the impregnation method. During the pyrolysis process, these exposed active atoms were thus easier to decompose directly into the high valence. Furthermore, the well developed interconnected networks of the ordered macro-mesopore structures of the 3DOM carbon would potentially afford much more internal surface to expose the active atoms. It was much reported that Mn⁴⁺ species and their redox processes were responsible for the high activity over the manganese-based catalysts in the low temperature NH₃-SCR reaction. And a high Mn⁴⁺ ratio would enhance the oxidation of NO to NO₂, which was beneficial to promote the low-temperature SCR activity.^{17, 52-55} Therefore, the higher atomic concentration of Mn⁴⁺ would play an important role in obtaining better low-temperature NO_x removal ability for the MnO_x/3DOMC catalyst than for the other two catalysts. On the other hand, the O1s spectrum is frequently used to identify the types of surface oxygen species in a particular oxide. The chemical environment of oxygen in metal oxide catalysts often has an important effect on their catalytic properties. Fig. 4 also shows the O1s spectra of the three catalysts. For all the catalysts, three deconvoluted peaks were observed, which were attributed to three types of oxygen species: the peak at BE of 529-530 eV was assigned to the lattice oxygen O²⁻ in Mn-O-Mn (denoted as O_β), the peak at BE of 531-532 eV was ascribed

to the surface oxygen ions with low coordination (denoted as O_{α}), such as O^{-} or O_2^{2-} belonging to the hydroxide (Mn-OH) or defective oxides, and the peak at a higher BE of above 533 eV corresponded to adsorbed water.^{53, 56-59} It was established that the O_{α} were more active than the O_{β} due to its higher mobility than the O_{β} .⁶⁰ As a result, the higher $O_{\alpha}/(O_{\alpha} + O_{\beta})$ ratio was favorable to the NH_3 -SCR reaction owing to the enhanced oxidation of NO to NO_2 . Based on the XPS, the concentrations of $O_{\alpha}/(O_{\alpha} + O_{\beta})$ over the $MnO_2/3DOMC$, MnO_x/NAC , and MnO_x/TiO_2 catalysts were calculated to be 14.1%, 3.8% and 10.1%, respectively (Table 2). Considering these results, as well as the manganese valence analysis, it was therefore reasonable to expect that the $MnO_x/3DOMC$ catalyst would potentially achieve better activity than the other two catalysts in the NH_3 -SCR reaction at low temperature.

Fig. 5 illustrates typical TEM images of the $MnO_x/3DOMC$, MnO_x/NAC , and MnO_x/TiO_2 catalysts. It was clearly seen in Fig. 5a that the $MnO_x/3DOMC$ possessed a high-quality 3DOM structure containing interconnected networks with overlapped pores. The macroporous diameter of the $MnO_x/3DOMC$ was ~200 nm, in good agreement with its SEM observation. A clearer observation in the partial magnified image in Fig. 5b revealed that MnO_x nanoparticles were highly distributed on the macropore walls of the 3DOM carbon scaffold. The sizes of MnO_x nanoparticles fell in the range of 2-4 nm, as seen by the tiny black spots. From the high-resolution TEM image in Fig. 5c, the high dispersion MnO_x on 3DOM carbon was much easier to be observed. Two crystal lattice fringes with a d -spacing of 0.239 and 0.418 nm corresponding to the (110) and (211) planes of MnO_2 respectively can be clearly

observed as well, whereas no significant crystalline plane of carbon was found, substantiating its amorphous nature. In addition, there were numerous mesopores with an average size of 5 nm randomly distributed in the macropore walls of the 3DOM carbon scaffold. The emergence of the mesopores could potentially enhance the capability of absorption and activation for gas reactant. Similar formation pathways have been discussed by other groups.^{42, 61} Differing greatly from the MnO_x/3DOMC, the TEM image in Fig. 5d displayed a relatively low dispersion of the MnO_x particles with sizes of 20-100 nm in the MnO_x/NAC. Similarly for the MnO_x/TiO₂, as shown in Fig. 5e, a large number of aggregates were formed.

The NH₃-TPD technique is often employed to determine the surface acid amount and strength of catalysts. The area of desorption peak is directly proportional to the acid amount and the peak position is correlated with the acid strength. Fig. 6 shows the NH₃-TPD profiles of the MnO_x/3DOMC, MnO_x/NAC, and MnO_x/TiO₂ catalysts. For the MnO_x/3DOMC, the NH₃ desorption profile exhibited three distinct desorption peaks centered at 247 °C, 365 °C, and 562 °C, assignable to the NH₃ desorbed by weak, medium and strong acid sites, respectively.^{62, 63} It was well accepted that the coordinated NH₃ molecular bound to the Lewis (L) acid sites was more thermally stable than the NH₄⁺ ions fixed on the Brønsted (B) acid sites.⁶⁴ It was therefore conjectured that the desorption peak at low temperature was assigned to physisorbed NH₄⁺ ions bound to the B acid sites, while the desorption peak at high temperature was associated with NH₃ molecular originating from the L acid sites.⁶⁵ On the other hand, pyridine is commonly used as a basic probe molecule for characterization of

both B and L acidic sites by FTIR spectroscopy. In order to ascertain the type of B or L acid, we further characterized the MnO_x/3DOMC by pyridine-DRIFTS. As shown in Fig. S3, the band at 1446 cm⁻¹ was typically attributed to pyridine bound to L acid sites, the band at 1487 cm⁻¹ was assigned to the L or B acid sites, and the band at 1540 cm⁻¹ was generally assigned to pyridine bound to B acid sites.^{66, 67} Evidently, the strong and medium L acid sites were the main acid sites in the MnO_x/3DOMC, whereas the peak belonging to B acid sites was relatively weak, indicating that only a small number of B acid sites were formed. For the MnO_x/NAC, there were two major NH₃ desorption peaks centered at 354 °C and 546 °C. Moreover, the overall curve shifted towards the low temperature region, indicating that the strength of acid sites on MnO_x/NAC became weaker than that on MnO_x/3DOMC. Meanwhile, the smaller area of desorption peaks of MnO_x/NAC also implied a lower number of acid sites on this catalyst. For the MnO_x/TiO₂, the NH₃ desorption peaks were relatively weak as compared with the other two samples, suggesting its shortage of acid sites. Such results indicated that the preparation method has a significant effect on the amount and the strength of the acidic sites on the catalysts. In our case, the MnO_x/3DOMC was derived from P-F phenolic resin, which contained various aromatic structures supplying enough strong acid sites.⁶⁸ On the other hand, it was reported that some oxides could increase the acidity of support remarkably.⁶⁹ The largest area of the desorption peaks of the MnO_x/3DOMC implied the most Brønsted and Lewis acid sites it possessed, which could be attributed to 3DOM carbon itself and the MnO_x nanoparticles on 3DOM carbon.

H₂-TPR is an ideal tool for investigating the reducibility of the MnO_x over the different supports. Fig. 7 records the H₂-TPR profiles of the MnO_x/3DOMC, MnO_x/NAC, and MnO_x/TiO₂ catalysts. It was reported that the reduction process of MnO_x took place in the following stepwise order: MnO₂ → Mn₂O₃ → Mn₃O₄ → MnO.^{57, 70} For the MnO_x/3DOMC, there was one strong reduction peak centered at 233 °C, assigned to the reduction of major MnO₂. For the MnO_x/NAC, the reduction peak of MnO₂ shifted to a higher temperature of 270 °C accompanying with the emergence of another obvious broad peak at 341 °C, which was correlated to the reduction of Mn₂O₃ phase. For the MnO_x/TiO₂, in addition to the peaks of the reduction of MnO₂ to Mn₂O₃ (281 °C) and Mn₂O₃ to Mn₃O₄ (376 °C), the third peak at 464 °C, indicative of the reduction Mn₃O₄ to MnO, was observed. Apparently, the reduction temperature of MnO₂ in the MnO_x/3DOMC catalyst was found to be lower than those in the MnO_x/NAC and MnO_x/TiO₂ catalysts, indicating the strongest reducibility of MnO₂ in the MnO_x/3DOMC catalyst. Furthermore, the larger area of the reduction peak of the MnO_x/3DOMC catalyst meant the higher consumption of H₂, suggesting that more active species were exposed in the MnO_x/3DOMC catalyst than in the other two catalysts. This was in very good agreement with the TEM observation and XPS analysis.

NH₃-SCR of NO_x

Fig. 8 exhibits the plots of NO conversion percentage versus reaction temperature from 50 to 300 °C for the MnO_x/3DOMC, MnO_x/NAC, and MnO_x/TiO₂ catalysts. The NO conversion increased first and then decreased with increasing reaction

temperature for all the catalysts. The catalytic activity of the MnO_x/3DOMC was much higher than those of the MnO_x/NAC and MnO_x/TiO₂. A nearly 100% NO conversion was achieved at 150 °C for the MnO_x/3DOMC while it needed 210 °C for the MnO_x/NAC. Compared with the MnO_x/3DOMC and MnO_x/NAC, the MnO_x/TiO₂ only completed 95 % NO conversion at 230 °C. Evidently, the MnO_x/3DOMC catalyst displayed the best catalytic performance. Based on the NO conversion at 100 °C, the TOF of the MnO_x/3DOMC was calculated to be $3.81 \times 10^{-4} \text{ s}^{-1}$, which was higher than that of the MnO_x/NAC ($1.79 \times 10^{-4} \text{ s}^{-1}$) and MnO_x/TiO₂ ($1.31 \times 10^{-4} \text{ s}^{-1}$). In addition, we also compared the TOF of the MnO_x/3DOMC with some reported counterparts of MnO_x-based NH₃-SCR catalysts. As tabulated in Table 3, our result for the MnO_x/3DOMC was much higher than those of the reported supported MnO_x catalysts.^{11, 14, 17, 71-79} The superior catalytic performance of the MnO_x/3DOMC was mainly ascribed to the followings. The 3DOM carbon was the basic scaffold providing good accessibility for mass transport of the NO, NH₃, and the corresponding product molecules, mechanical stability, and large surface area for absorbing reactants in the feed gas. The highly dispersed MnO_x nanoparticles were directly introduced into carbon matrix, giving rise to more active sites and enabling the fast mass transfer for the reaction. In addition, the enhanced redox and acidic abilities of the MnO_x/3DOMC played important roles in the NH₃-SCR reaction.

Long-term stability is an important merit for catalysts. Meanwhile, since water vapor and/or SO₂ are inevitable components of exhaust gas and may cause severe deactivation of catalysts for the NH₃-SCR reaction, it is also necessary to study the

water vapor resistance and/or SO₂ tolerance of catalysts. Fig. 9 indicates the stability and the effects of water vapor and/or SO₂ on NO conversion over the MnO_x/3DOMC, MnO_x/NAC, and MnO_x/TiO₂ catalysts. During a 48 h period at 190 °C (Fig. 9a), the MnO_x/3DOMC preserved a high NO conversion at ~98% with almost negligible activity decay. Unfortunately, the NO conversions over the MnO_x/NAC and MnO_x/TiO₂ gradually faded with reaction time. After the continuous 48 h reaction, the 3DOM structure of the MnO_x/3DOMC catalyst was still well-maintained with partial pore collapse to some extent, and the whole structural integrity remained considerably (Fig. 9e), implying that the long-term reaction did not spoil the structure of the catalyst and the high NO conversion could be further well preserved. The NH₃-TPD profile after the long-term test shown in Fig. S4 also verified that there were indiscernible changes of the amount of acid sites and acid strength in the MnO_x/3DOMC catalyst. When 5 v.% water vapor was introduced into the feed gases (Fig. 9b), all the NO conversions over the three catalysts decreased during the test period. The fall range was ~3.4 % for MnO_x/3DOMC, ~5.0% for MnO_x/NAC, and ~9.3% for MnO_x/TiO₂, respectively, suggesting that the MnO_x/3DOMC had a higher capacity for water vapor-resistance. After the water vapor was discontinued from the feed gases, all the NO conversions were almost restored to their originals, indicating that the inhibition effect of water vapor over the three catalysts was reversible. This was in good line with the reported results that the inhibition of water vapor resulted from the competitive adsorption between water and ammonia on the active sites of the catalyst's surface, which was reversible.^{80, 81} When 200 ppm of SO₂ was added to the

feed gases (Fig. 9c), the NO conversion over the MnO_x/3DOMC decreased slightly from initial 99 % to 94 %, then presented a gradually recovery trend during the test period. By contrast, the presence of SO₂ caused a significant decrease of NO conversion over the MnO_x/NAC and MnO_x/TiO₂ by 9 and 15%, respectively. After excluding SO₂ in the feed gases, the conversions of NO over the MnO_x/NAC and MnO_x/TiO₂ gradually restored to a certain extent, but still were less than their initial values, and finally returned to 81 and 58%, respectively. This substantiated that the MnO_x/3DOMC had a stronger resistance to SO₂. The NH₃-TPD profile after the SO₂-resistance test shown in Fig. S4 confirmed the remarkable increases in the amount of acid sites and acid strength in the MnO_x/3DOMC catalyst. This was likely due to the increasing acidity of the catalyst by potential SO₂ sulfuration, and implied that the acidity was not the only factor for the MnO_x/3DOMC catalyst to determine the SCR performance. It was reported that the SO₂ poisoning and deactivation to catalyst was usually related to the generation of ammonium sulfate species and deposition on the catalyst surface, blocking the active sites of the catalyst surface. And some MnO_x-based catalysts resistance to SO₂ could be enhanced due to the strong interaction between MnO_x and the support with the inhibition of manganese sulfate formation on catalyst surface.^{82, 83} In our case, the present MnO_x nanoparticles formed with the dual-CCTS were mainly imbedded in or anchored on the carbon walls, which would not only produce highly dispersed MnO_x nanoparticles in the 3DOMC matrix, but it could also create intimate contacts and strong interactions between the MnO_x nanoparticles and the carbon support. Based on this point, such

unique feature of the MnO_x/3DOMC obviously helped to improve its SO₂ resistance ability. In addition, the effect of coexistence of water vapor and SO₂ was investigated. When 5 v.% water vapor and 200 ppm SO₂ were together introduced into the feed gases (Fig. 9d), the variation of NO conversion of the three catalysts were similar as those in the SO₂-existence model. All the NO conversions exhibited a trend of first decrease, then gradual recovery to a certain extent but less than their initial values, and finally returned to some stable values during the test period. This was likely stemmed from the synergistic inhibition effect of water vapor and SO₂.

The excellent catalytic performance of the MnO_x/3DOMC catalyst was approximately described as the Fig. 10 demonstrating. In the macro aspect, the MnO_x/3DOMC was hierarchically porous structure. There were numerous additional mesopores in the macropore walls of the well-developed interconnected monolithic MnO_x/3DOMC framework. Moreover, the MnO_x nanoparticles were highly dispersed in the macropore walls where intimate contacts and strong interactions between the MnO_x nanoparticles and the carbon support could be well yielded. These features were favorable to provide easier mass transport and more accessible internal surface area for the reaction, increase the number of active sites, and prevent the MnO_x nanoparticles aggregation and growth during reaction. Meanwhile in the microcosmic aspect, the NH₃-SCR of NO_x over the MnO_x/3DOMC catalyst was possibly described as the following five underlying reactions (Fig. 10). Reaction (1) was the adsorption of gaseous ammonia on the acid sites (*i.e.* B acid sites and L acid sites) to form adsorbed ammonia species including ionic NH⁴⁺ and coordinated NH₃. Reaction (2)

was the activation of adsorbed ammonia species by Mn^{4+} to form amide species ($-\text{NH}_2$). Reaction (3) was the oxidation of NO to NO_2 . Then, gaseous NO and NO_2 were reduced by $-\text{NH}_2$ on the surface to form N_2 and H_2O *via* reaction (4). Reaction (5) was the re-oxidization of formed Mn^{3+} .

Conclusions

We have successfully prepared the $\text{MnO}_x/3\text{DOMC}$ nanocomposite *via* a simple multi-component infiltration of 3D PMMA templates followed by a direct pyrolysis process. The integration of 3DOM carbon and MnO_x enables such a nanocomposite to possess high MnO_x dispersion and strong interaction between the two components. As a catalyst, the $\text{MnO}_x/3\text{DOMC}$ nanocomposite displayed better low-temperature NH_3 -SCR activity and a more extensive operating temperature window than the MnO_x/NAC and $\text{MnO}_x/\text{TiO}_2$ catalysts prepared by a conventional impregnation method. In addition, the $\text{MnO}_x/3\text{DOMC}$ nanocomposite also presented favourable stability, water vapor, and/or SO_2 resistance. Such excellent catalytic behavior can be attributed to the positive synergetic contributions of the $\text{MnO}_x/3\text{DOMC}$ nanocomposite, including easy mass transport, large accessible surface area, highly dispersed MnO_x nanoparticles on the 3DOM carbon substrate, and the enhanced redox and acidic properties. These results should deepen the understanding of the role of combining hierarchical ordered macrostructure with MnO_x in catalysis. Moreover, this work conceptually provides a way for tailoring/designing 3DOM metal (oxide)-carbon nanocomposites to many different catalysts for various catalytic reactions, and thus is worthy of further exploration.

Acknowledgements

This work was financially supported by the National Natural Science Foundation of China (No.21071072) and the Doctoral Program Foundation of Liaoning Province (No. 20091047). We thank Mr. Gang Zhao (College of Environmental Science and Engineering, Dalian Maritime University) for running XPS measurements.

Notes and references

- 1 Z. M. Liu, J. H. Li and S. I. Woo, *Energy Environ. Sci.*, 2012, **5**, 8799-8814.
- 2 F. Klingstedt, K. Arve, K. Eränen and D. Y. Murzin, *Acc. Chem. Res.*, 2006, **39**, 273-282.
- 3 P. Forzatti, I. Nova and E. Tronconi, *Ind. Eng. Chem. Res.*, 2010, **49**, 10386-10391.
- 4 P. G. W. A. Kompio, A. Brückner, F. Hipler, G. Auer, E. Löffler and W. Grünert, *J. Catal.*, 2012, **286**, 237-247.
- 5 P. G. Smirniotis, D. A. Peña and B. S. Uphade, *Angew. Chem. Int. Ed.*, 2001, **40**, 2479-2482.
- 6 G. S. Qi and R. T. Yang, *Appl. Catal. B*, 2003, **44**, 217-225.
- 7 W. Tian, H. S. Yang, X. Y. Fan and X. B. Zhang, *J. Hazard. Mater.*, 2011, **188**, 105-109.
- 8 X. F. Tang, J. H. Li, L. Sun and J. M. Hao, *Appl. Catal. B*, 2010, **99**, 156-162.
- 9 P. Maitarad, D. S. Zhang, R. H. Gao, L. Y. Shi, H. R. Li, L. Huang, T. Rungrotmongkol and J. P. Zhang, *J. Phys. Chem. C*, 2013, **117**, 9999-10006.
- 10 F. D. Liu, W. P. Shan, Z. H. Lian, L. J. Xie, W. W. Yang and H. He, *Catal. Sci.*

- Technol.*, 2013, **3**, 2699-2707.
- 11 X. R. Lou, P. F. Liu, J. Li, Z. Li and K. He, *Appl. Surf. Sci.*, 2014, **307**, 382-387.
- 12 Y. J. Kim, H. J. Kwon, I. S. Nam, J. W. Choung, J. K. Kil, H. J. Kim, M. S. Cha and G. K. Yeo, *Catal. Today*, 2011, **151**, 244-250.
- 13 J. L. Xie, D. Fang, F. He, J. F. Chen, Z. B. Fu and X. L. Chen, *Catal. Commun.*, 2012, **28**, 77-81.
- 14 S. J. Yang Y. W. Fu, Y. Liao, S. C. Xiong, Z. Qu, N. Q. Yan and J. H. Li, *Catal. Sci. Technol.*, 2014, **4**, 224-232.
- 15 M. Casapu, O. Kröcher and M. Elsener, *Appl. Catal. B*, 2009, **88**, 413-419.
- 16 X. Tang, J. Hao, H. Yi and J. Li, *Catal. Today*, 2007, **126**, 406-411.
- 17 L. S. Wang, B. C. Huang, Y. X. Su, G. Y. Zhou, K. L. Wang, H. C. Luo and D. Q. Ye, *Chem. Eng. J.*, 2012, **192**, 232-241.
- 18 X. Wang, Y. Y. Zheng, Z. Xu, X. L. Wang and X. P. Chen, *RSC Adv.*, 2013, **3**, 11539-11542.
- 19 X. M. Wang, Y. N. Wang, L. Feng, P. G. Liu and X. Zhang, *Chem. Eng. J.*, 2012, **203**, 251-258.
- 20 X. Zhang, G. H. Li, H. Q. Zhang, X. M. Wang, J. Y. Qu, P. G. Liu and Y. N. Wang, *Soft Matter*, 2013, **9**, 6159-6166.
- 21 S. M. Sun, W. Z. Wang and L. Zhang, *J. Mater. Chem.*, 2012, **22**, 19244-19249.
- 22 K. M. Ji, H. X. Dai, J. G. Deng, L. Y. Song, B. Z. Gao, Y. Wang and X. W. Li, *Appl. Catal. B*, 2013, **129**, 539-548.
- 23 D. L. Ma, Z. Y. Cao, H. G. Wang, X. L. Huang, L. M. Wang and X. B. Zhang,

- Energy Environ. Sci.*, 2012, **5**, 8538-8542.
- 24 Z. Liu, J. H. Mi, Y. Yang, X. L. Tan and C. Lv, *Electrochim. Acta*, 2014, **115**, 206-215.
- 25 Y. Chen, Y. J. Zhu and Z. G. Chen, *Thin Solid Films*, 2013, **539**, 122-126.
- 26 M. A. Al-Daous and A. Stein, *Chem. Mater.*, 2003, **15**, 2638-2645.
- 27 J. Q. Zhao, P. Wan, J. Xiang, T. Tong, L. Dong, Z. N. Gao, X. Y. Shen and H. Tong, *Micropor. Mesopor. Mater.*, 2011, **138**, 200-206.
- 28 A. Vu and A. Stein, *Chem. Mater.*, 2011, **23**, 3237-3245.
- 29 D. Z. Han, X. Li, L. Zhang, Y. H. Wang, Z. F. Yan and S. M. Liu, *Micropor. Mesopor. Mater.*, 2012, **158**, 1-6.
- 30 C. M. A. Parlett, K. Wilson and A. F. Lee, *Chem. Soc. Rev.*, 2013, **42**, 3876-3893.
- 31 A. Stein, B. E. Wilson and S. G. Rudisill, *Chem. Soc. Rev.*, 2013, **42**, 2763-2803.
- 32 H. Arandiyani, H. X. Dai, J. G. Deng, Y. X. Liu, B. Y. Bai, Y. Wang, X. W. Li, S. H. Xie and J. H. Li, *J. Catal.*, 2013, **307**, 327-339.
- 33 N. D. Petkovich and A. Stein, *Chem. Soc. Rev.*, 2013, **42**, 3721-3739.
- 34 H. J. Wan, B. S. Wu, H. W. Xiang and Y. W. Li, *ACS Catal.*, 2012, **2**, 1877-1883.
- 35 Y. Liu, W. Y. Yao, X. L. Cao, X. L. Weng, Y. Wang, H. Q. Wang and Z. B. Wu, *Appl. Catal. B*, 2014, **160-161**, 684-691.
- 36 C. He, J. R. Li, X. Y. Zhang, L. Q. Yin, J. S. Chen and S. K. Gao, *Chem. Eng. J.*, 2012, **180**, 46-56.
- 37 H. N. Li, L. Zhang, H. X. Dai and H. He, *Inorg. Chem.*, 2009, **48**, 4421-4434.
- 38 Y. Meng, D. Gu, F. Q. Zhang, Y. F. Shi, H. F. Yang, Z. Li, C. Z. Yu, B. Tu and D.

- Y. Zhao, *Angew. Chem. Int. Ed.*, 2005, **44**, 7053-7059.
- 39 C. Z. Sun, J. Zhu, Y. Y. Lv, L. Qi, B. Liu, F. Gao, K. Q. Sun, L. Dong and Y. Chen, *Appl. Catal. B*, 2011, **103**, 206-220.
- 40 Z. Liu, A. Q. Wang, X. D. Wang and T. Zhang, *Catal. Today*, 2008, **137**, 162-166.
- 41 Z. Liu, Y. Yang, J. H. Mi, X. L. Tan and Y. Song, *Catal. Commun.*, 2012, **21**, 58-62.
- 42 R. Z. Zhang, H. X. Dai, Y. C. Du, L. Zhang, J. G. Deng, Y. S. Xia, Z. X. Zhao, X. Meng and Y. X. Liu, *Inorg. Chem.*, 2011, **50**, 2534-2544.
- 43 H. Zhang, H. X. Dai, Y. X. Liu, J. G. Deng, L. Zhang and K. M. Ji, *Mater. Chem. Phys.*, 2011, **129**, 586-593.
- 44 Y. X. Liu, H. X. Dai, Y. C. Du, J. G. Deng, L. Zhang, Z. X. Zhao and C. T. Au, *J. Catal.*, 2012, **287**, 149-160.
- 45 Z. X. Zhao, H. X. Dai, J. G. Deng, Y. C. Du, Y. X. Liu and L. Zhang, *Micropor. Mesopor. Mater.*, 2012, **163**, 131-139.
- 46 H. Arandiyani, H. X. Dai, J. G. Deng, Y. X. Liu, B. Y. Bai, Y. Wang, X. W. Li, S. H. Xie and J. H. Li, *J. Catal.*, 2013, **307**, 327-339.
- 47 K. M. Ji, H. X. Dai, J. G. Deng, H. Y. Jiang, L. Zhang, H. Zhang and Y. J. Cao, *Chem. Eng. J.*, 2013, **214**, 262-271.
- 48 Y. C. Wei, Z. Zhao, T. Li, J. Liu, A. J. Duan and G. Y. Jiang, *Appl. Catal. B*, 2014, **146**, 57-70.
- 49 J. J. Xu, Z. L. Wang, D. Xu, F. Z. Meng and X. B. Zhang, *Energy Environ. Sci.*, 2014, **7**, 2213-2219.

- 50 C. D. Wanger, W. M. Riggs, L. E. Davis, J. F. Moulder and G. E. Muilenberg, *Handbook of X-ray Photoelectron Spectroscopy*, PerkinElmer, Eden Prairie, 1978.
- 51 Z. H. Chen, Q. Yang, H. Li, X. H. Li, L. F. Wang and S. C. Tsang, *J. Catal.*, 2010, **276**, 56-65.
- 52 M. Kang, E. D. Park, J. M. Kim and J. E. Yie, *Appl. Catal. A*, 2007, **327**, 261-269.
- 53 F. D. Liu, H. He, Y. Ding and C. B. Zhang, *Appl. Catal. B*, 2009, **93**, 194-204.
- 54 B. Thirupathi and P. G. Smirniotis, *J. Catal.*, 2012, **288**, 74-83.
- 55 A. Sultana, M. Sasaki and H. Hamada, *Catal. Today*, 2012, **185**, 284-289.
- 56 A. E. Fischer, K. A. Pettigrew, D. R. Rolison, R. M. Stroud and J. W. Long, *Nano Lett.*, 2007, **7**, 281-286.
- 57 P. R. Ettireddy, N. Ettireddy, S. Mamedov, P. Boolchand and P. G. Smirniotis, *Appl. Catal. B*, 2007, **76**, 123-134.
- 58 Y. S. Wu, Y. X. Zhang, M. Liu and Z. C. Ma, *Catal. Today*, 2010, **153**, 170-175.
- 59 E. Park, S. Chin, Y. S. Kim, G. N. Bae and J. Jurng, *Powder Technol.*, 2013, **233**, 131-136.
- 60 F. D. Liu and H. He, *J. Phys. Chem. C*, 2010, **114**, 16929-16936.
- 61 W. B. Sui, J. T. Zheng, Z. Yang and M. B. Wu, *Mater. Lett.*, 2011, **65**, 2534-2536.
- 62 L. Chmielarz, P. Kustrowski, M. Zbroja, B. Gil-Knap, J. Datka and R. Dziembaj, *Appl. Catal. B*, 2004, **53**, 47-61.
- 63 Y. S. Shen and S. M. Zhu, *Catal. Sci. Technol.*, 2012, **2**, 1806-1810.

- 64 R. B. Jin, Y. Liu, Z. B. Wu, H. Q. Wang and T. T. Gu, *Chemosphere*, 2010, **78**, 1160-1166.
- 65 S. Roy, B. Viswanath, M. S. Hegde and G. Madras, *J. Phys. Chem. C*, 2008, **112**, 6002-6012.
- 66 J. A. Lercher, C. Grundling, G. E. Mirth, *Catal. Today*, 1996, **27**, 353-376.
- 67 M. Akçay, *Appl. Catal. A*, 2005, **294**, 156-160.
- 68 C. Moreno-Castilla and F. J. Maldonado-Hódar, *Carbon*, 2005, **43**, 455-465.
- 69 K. Keyvanloo, A. Mohamadalizadeh and J. Towfighi, *Appl. Catal. A*, 2012, **417-418**, 53-58.
- 70 T. Mishra, P. Mohapatra and K. M. parida, *Appl. Catal. B*, 2008, **79**, 279-285.
- 71 E. Park, S. Chin, J. Jeong and J. Jurng, *Micropor. Mesopor. Mater.*, 2012, **163**, 96-101.
- 72 M. Stanciulescu, G. Caravaggio, A. Dobri, J. Moir, R. Burich, J. P. Charland and P. Bultink, *Appl. Catal. B*, 2012, **123-124**, 229-240.
- 73 J. H. Ko, S. H. Park, J. K. Jeon, S. S. Kim, S. C. Kim, J. M. Kim, D. Chang and Y. K. Park, *Catal. Today*, 2012, **185**, 290-295.
- 74 B. X. Shen, X. P. Zhang, H. Q. Ma, Y. Yao and T. Liu, *J. Environ. Sci.*, 2013, **25**, 791-800.
- 75 B. X. Shen, Y. Y. Wang, F. M. Wang and T. Liu, *Chem. Eng. J.*, 2014, **236**, 171-180.
- 76 S. W. Pan, H. C. Luo, L. Li, Z. L. Wei and B. C. Huang, *J. Mol. Catal. A*, 2013, **377**, 154-161.

- 77 L. Xu, X. S. Li, M. Crocker, Z. S. Zhang, A. M. Zhu and C. Shi, *J. Mol. Catal. A*, 2013, **378**, 82-90.
- 78 S. M. Lee, K. H. Park and S. C. Hong, *Chem. Eng. J.*, 2012, **195-196**, 323-331.
- 79 T. T. Gu, R. B. Jin, Y. Liu, H. F. Liu, X. L. Weng and Z. B. Wu, *Appl. Catal. B*, 2013, **129**, 30-38.
- 80 I. Giakoumelou, C. Fountzoula, C. Kordulis and S. Boghosian, *J. Catal.*, 2006, **239**, 1-12.
- 81 X. L. Mou, B. S. Zhang, Y. Li, L. D. Yao, X. J. Wei, D. S. Su and W. J. Shen, *Angew. Chem. Int. Ed.*, 2012, **51**, 2989-2993.
- 82 J. H. Huang, Z. Q. Tong, Y. Huang and J. F. Zhang, *Appl. Catal. B*, 2008, **78**, 309-314.
- 83 Z. B. Wu, R. B. Jin, H. Q. Wang and Y. Liu, *Catal. Commun.*, 2009, **10**, 935-939.

Tables:**Table 1** – Textural properties of the three catalysts

Catalyst	S_{BET} ($\text{m}^2 \text{g}^{-1}$)	V_{meso} ($\text{cm}^3 \text{g}^{-1}$)	V_{micro} ($\text{cm}^3 \text{g}^{-1}$)	V_{p} ($\text{cm}^3 \text{g}^{-1}$)	Mn content (wt.%)
MnO _x /3DOMC	656	0.36	0.04	0.43	7.1
MnO _x /NAC	659	0.10	0.26	0.38	7.3
MnO _x /TiO ₂	68	0.05	0.01	0.11	7.4

Table 2 – XPS results of the three catalysts

Catalyst	$\text{Mn}^{4+}/(\text{Mn}^{2+} + \text{Mn}^{3+} + \text{Mn}^{4+})$ (%)	Mn (at.%)	Mn^{4+} (at.%)	Mn (wt.%)	$\text{O}_{\alpha}/(\text{O}_{\alpha} + \text{O}_{\beta})$ (%)	O (at.%)	O_{α} (at.%)
MnO _x /3DOMC	91	1.65	1.50	6.8	80.4	17.55	14.1
MnO _x /NAC	76	1.00	0.76	4.2	29.3	13.10	3.8
MnO _x /TiO ₂	49	1.60	0.78	2.5	26.1	38.6	10.1

Table 3 – TOF comparison for NH₃-SCR of NO_x over various MnO_x-based catalysts

Catalyst	Mn content (wt.%) by XPS	Composition of feed gas		GHSV (h ⁻¹)	Calculation temperature (°C)	TOF (s ⁻¹)	Ref.
		NO + NH ₃ (ppm)	O ₂ (vol.%)				
MnO_x/3DOMC	6.8	1000 + 1000	5	36000	100	3.81 × 10⁻⁴	This work
MnO _x /NAC	4.2	1000 + 1000	5	36000	100	1.79 × 10 ⁻⁴	This work
MnO _x /TiO ₂	2.5	1000 + 1000	5	40000	100	1.31 × 10 ⁻⁴	This work
MnZ-3	16.76	600 + 600	4.5	36000	100	7.98 × 10 ⁻⁵	[11]
MnO _x /TiO ₂	5	500 + 500	2	75000	100	4.08 × 10 ⁻⁵	[14]
MnO _x /MWCNTs	10	1000 + 1000	5	40000	100	2.57 × 10 ⁻⁴	[17]
Mn-MA/Ti-CVC	23.4	500 + 500	5	30000	100	4.89 × 10 ⁻⁶	[71]
MnCBV	3.5	500 + 500	5	80000	150	9.34 × 10 ⁻⁵	[72]
MnO _x /Al ₂ O ₃ -TiO ₂	8.2	500 + 500	5	80000	100	2.49 × 10 ⁻⁵	[72]
MnO _x /CZO	25.74	1000 + 1000	<5	6000	100	2.29 × 10 ⁻⁵	[73]
MnO _x /CeO ₂	7.22	600 + 660	6	45000	100	1.65 × 10 ⁻⁴	[74]
MnO _x /CeO ₂ -ZrO ₂	9.4	600 + 600	3	30000	100	1.39 × 10 ⁻⁴	[75]
MnO _x /MWCNTs	10	1000 + 1000	5	40000	100	5.90 × 10 ⁻⁵	[76]
MnO _x /CeO ₂	20	1000 + 1000	3	50000	100	2.04 × 10 ⁻⁴	[77]
MnO _x /CeO ₂ -TiO ₂	20	200 + 200	8	60000	120	2.63 × 10 ⁻⁵	[78]
(Ca)MnO _x /TiO ₂	23.58	650 + 650	3	75000	100	7.39 × 10 ⁻⁵	[79]

Figure captions:

- Fig. 1.** SEM images of: (a) the PMMA template; (b) the MnO_x/3DOMC catalyst.
- Fig. 2.** XRD patterns of the MnO_x/3DOMC, MnO_x/NAC, and MnO_x/TiO₂ catalysts.
- Fig. 3.** Nitrogen adsorption-desorption isotherms and corresponding pore size distributions of the MnO_x/3DOMC, MnO_x/NAC, and MnO_x/TiO₂ catalysts.
- Fig. 4.** XPS spectra for: Mn2p and O1s of the MnO_x/3DOMC, MnO_x/NAC, and MnO_x/TiO₂ catalysts.
- Fig. 5.** TEM images of: (a) (b) the MnO_x/3DOMC catalyst at low and high magnification; (c) the MnO_x/NAC catalyst; (d) the MnO_x/TiO₂ catalyst.
- Fig. 6.** NH₃-TPD profiles of the MnO_x/3DOMC, MnO_x/NAC, and MnO_x/TiO₂ catalysts.
- Fig. 7.** H₂-TPR profiles of the MnO_x/3DOMC, MnO_x/NAC, and MnO_x/TiO₂ catalysts.
- Fig. 8.** NO conversions over the MnO_x/3DOMC, MnO_x/NAC, and MnO_x/TiO₂ catalysts.
Reaction conditions: 1000 ppm of NO, 1000 ppm of NH₃, 5% of O₂, He balance.
- Fig. 9.** (a-d) Stability tests and effect(s) of water vapor (and/or SO₂) on NO conversion over the MnO_x/3DOMC (■), MnO_x/NAC (●), and MnO_x/TiO₂ (▲) catalysts.
Reaction conditions: 190 °C, 1000 ppm of NO, 1000 ppm of NH₃, 5% of O₂, 5% of water vapor, and/or 200 ppm of SO₂, He balance. (e) SEM image of the MnO_x/3DOMC catalyst after completing 48 h reaction.
- Fig. 10.** The proposed reaction mechanism for NH₃-SCR of NO_x over the MnO_x/3DOMC catalyst.

Figures:

Fig. 1.

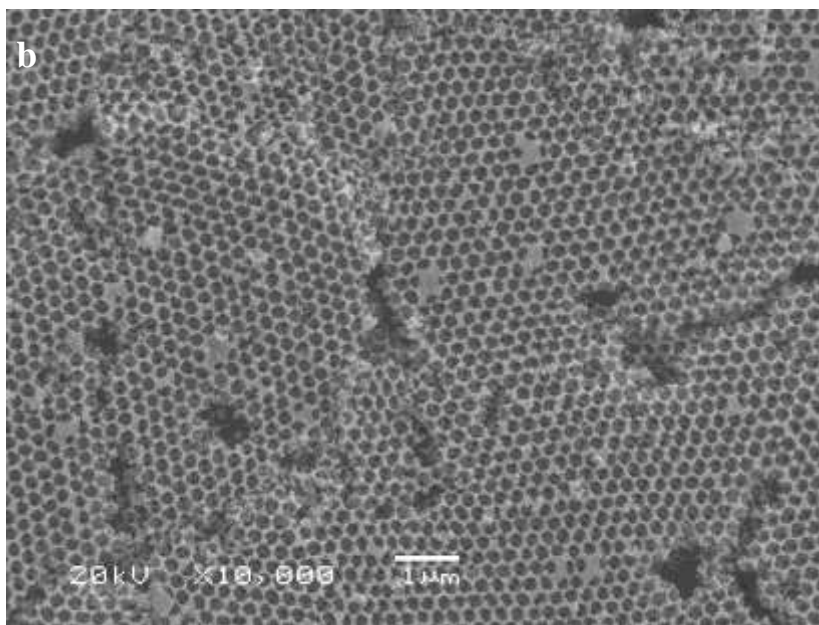
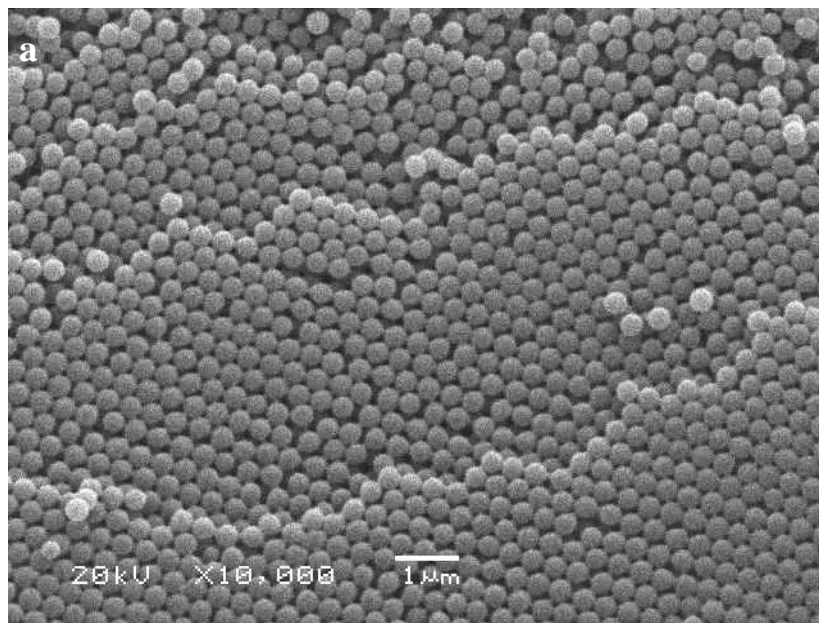


Fig. 2.

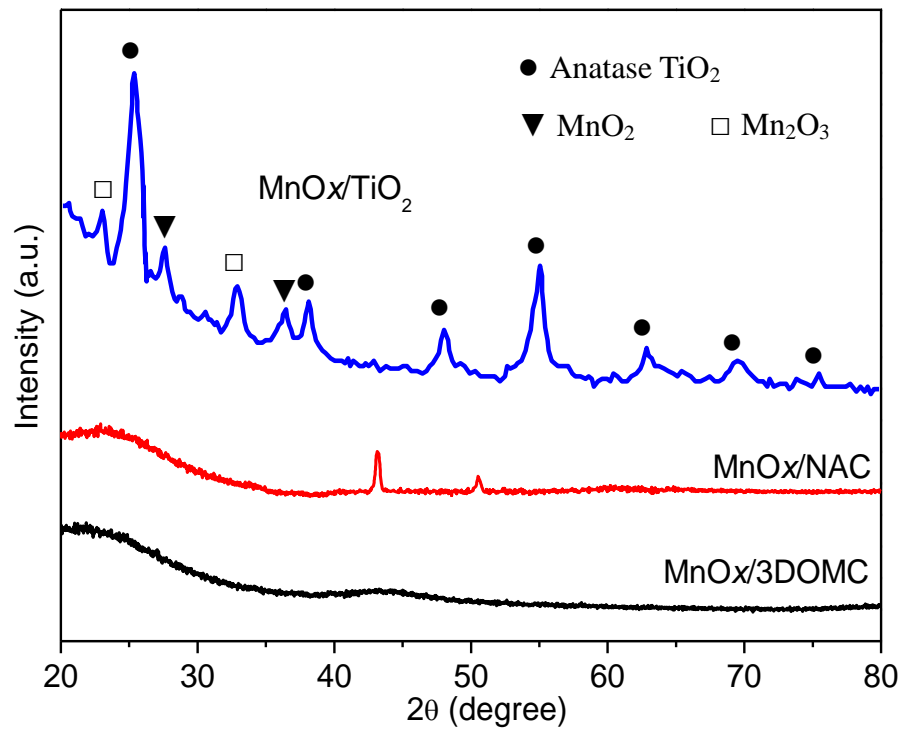
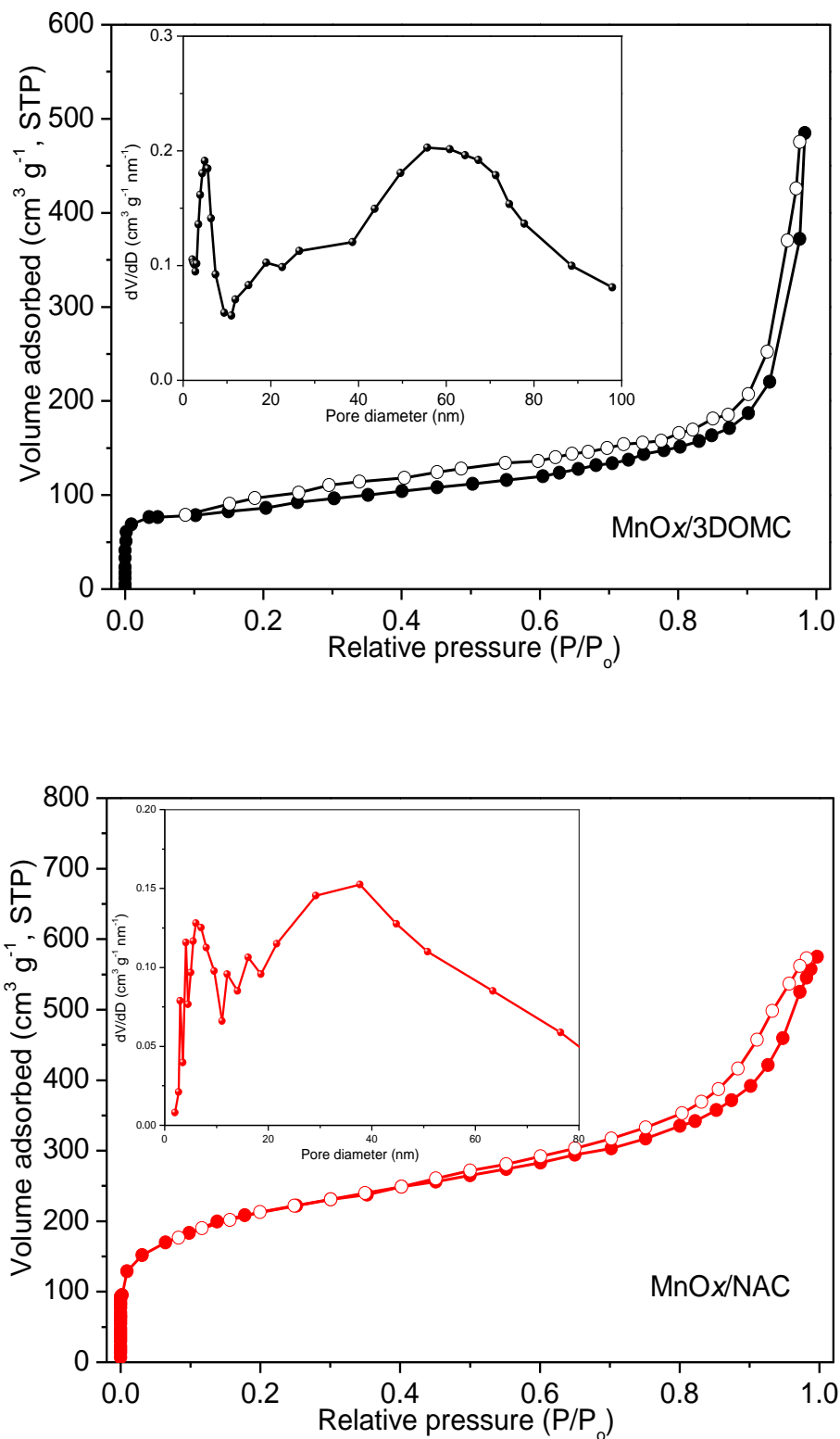


Fig. 3.



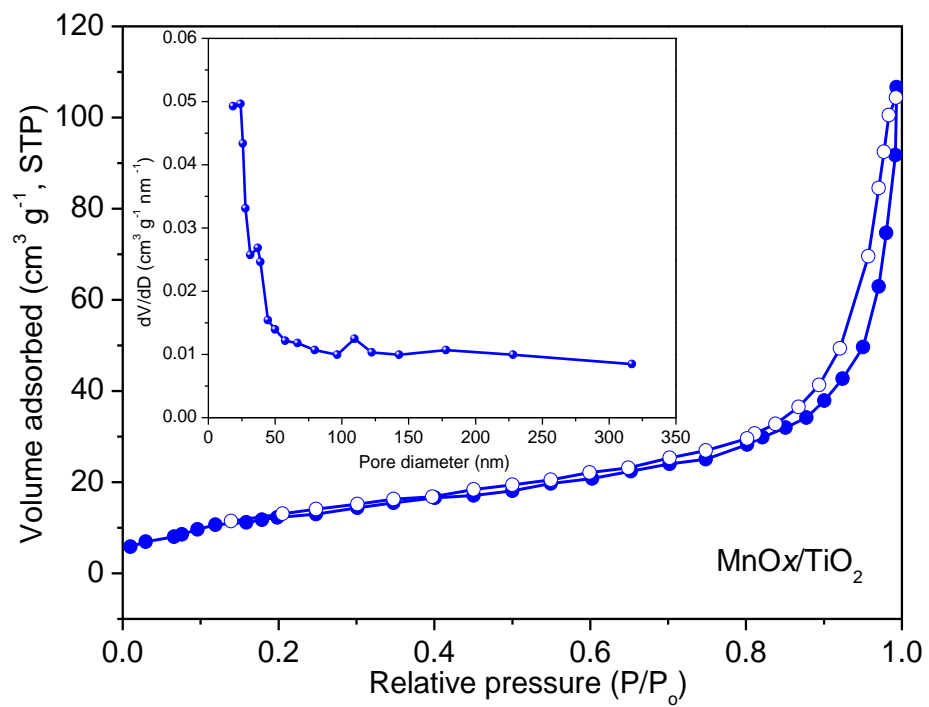
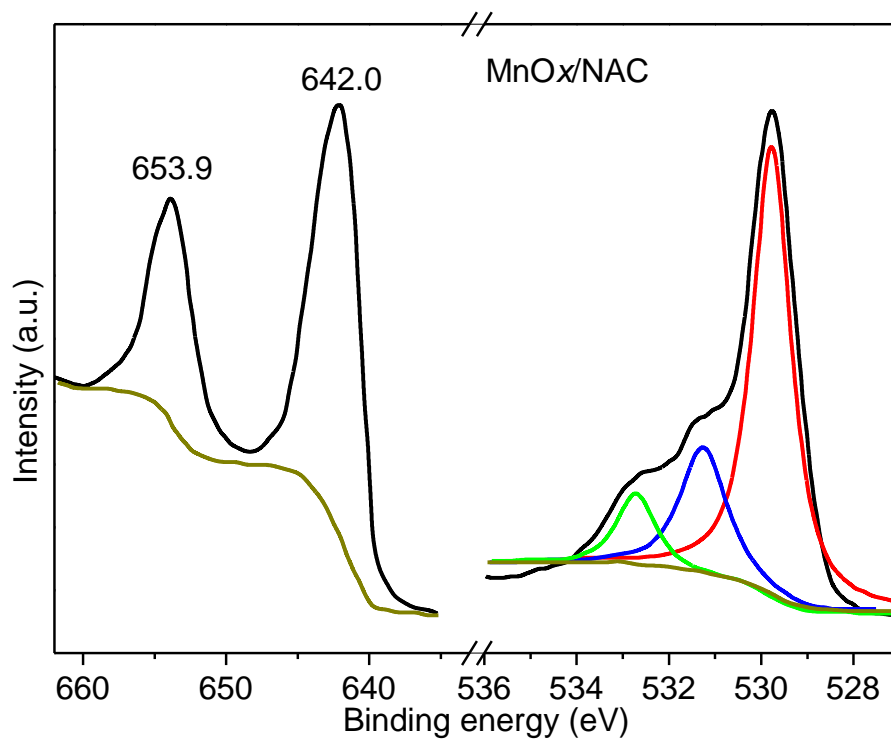
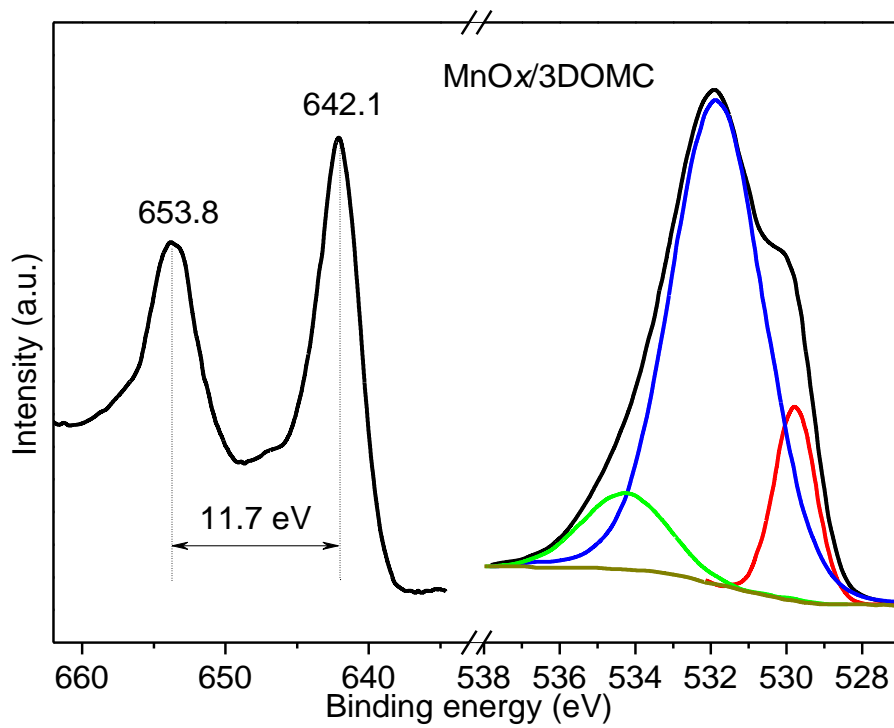


Fig. 4.



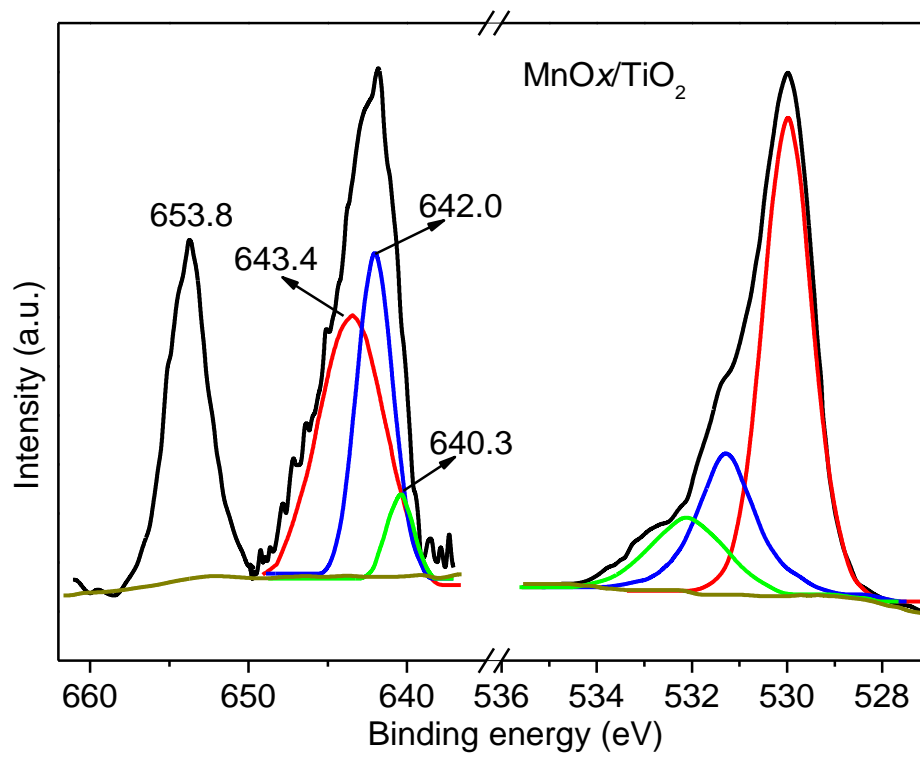
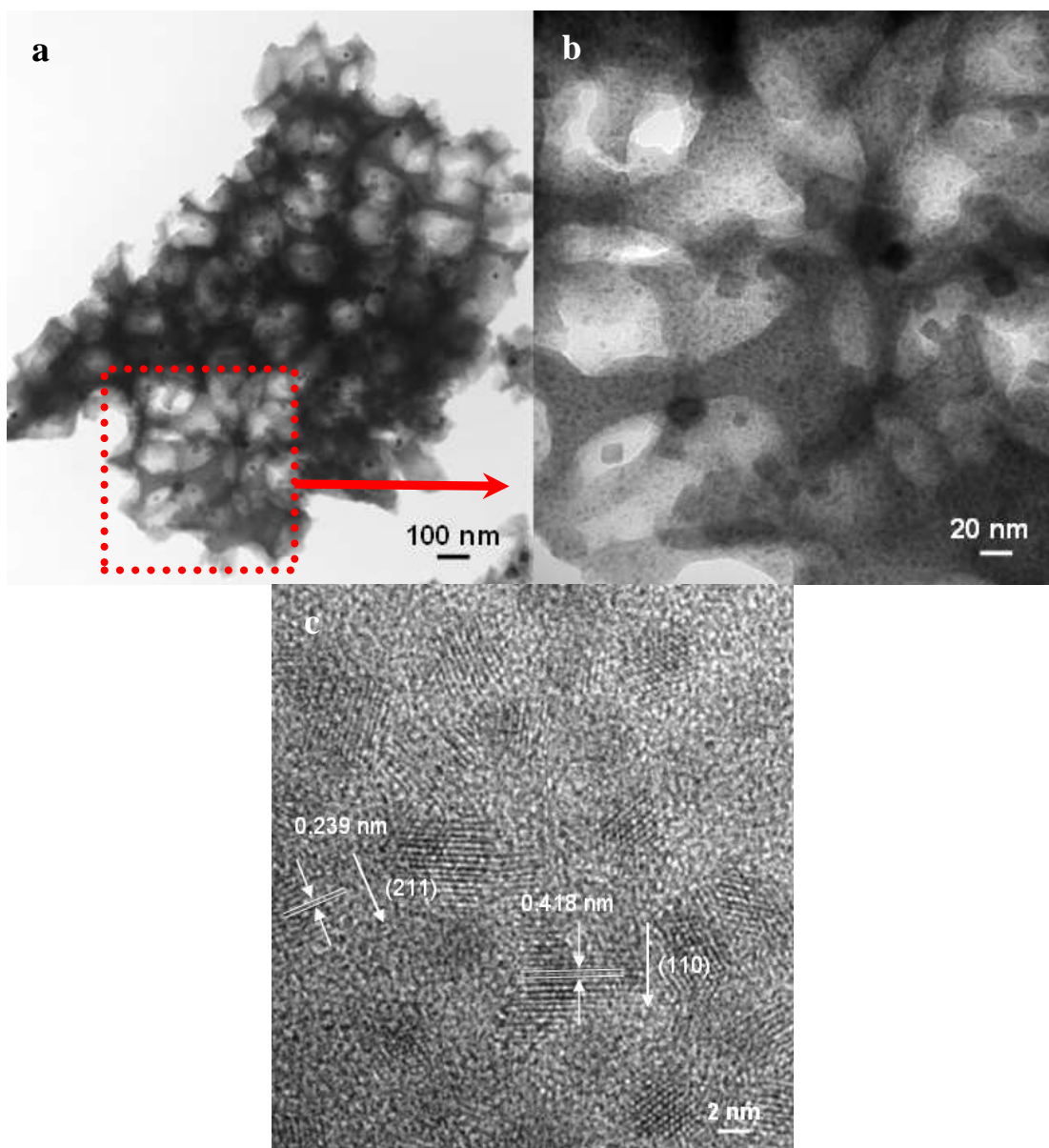


Fig. 5.



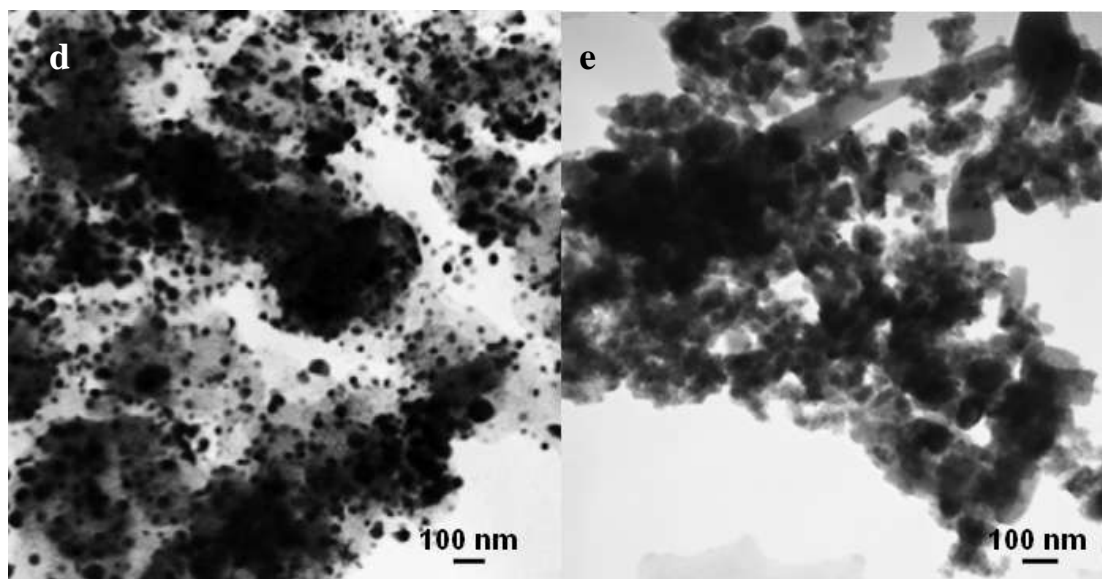


Fig. 6.

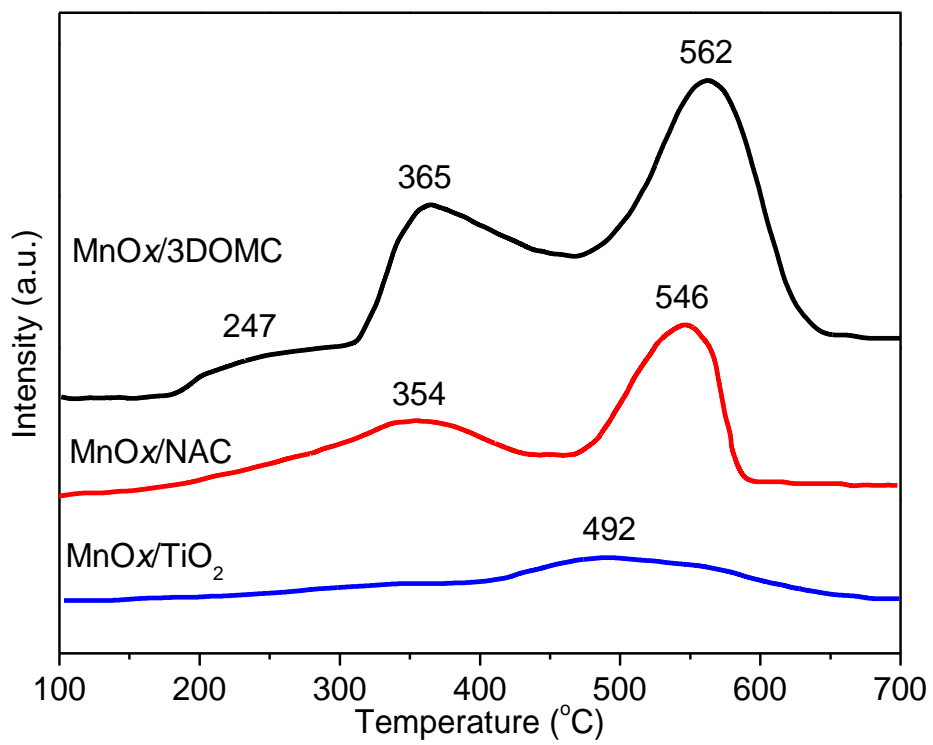


Fig. 7.

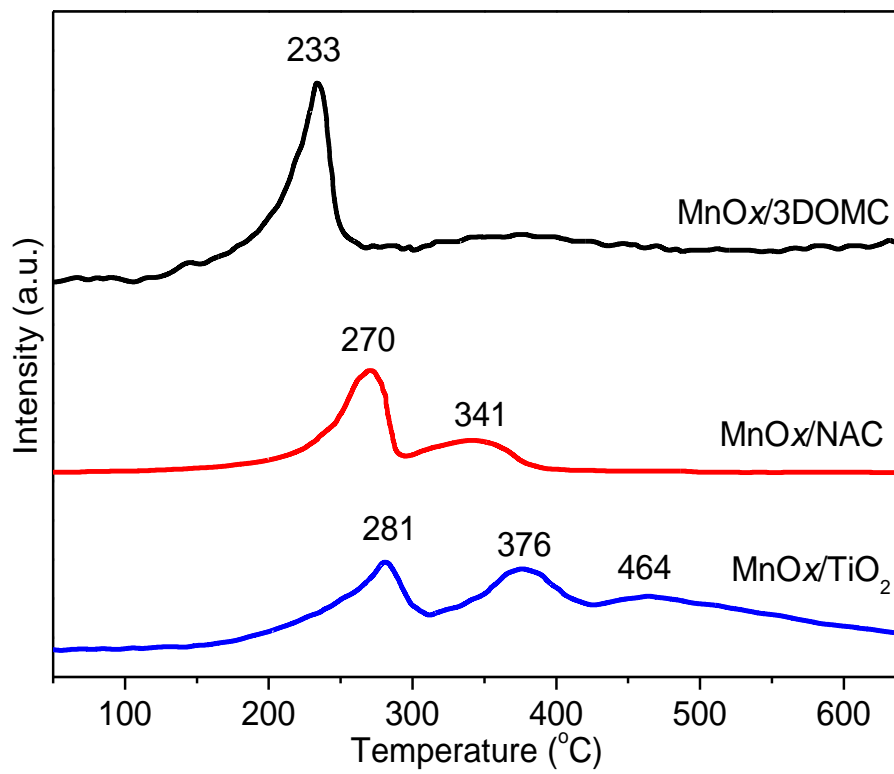


Fig. 8.

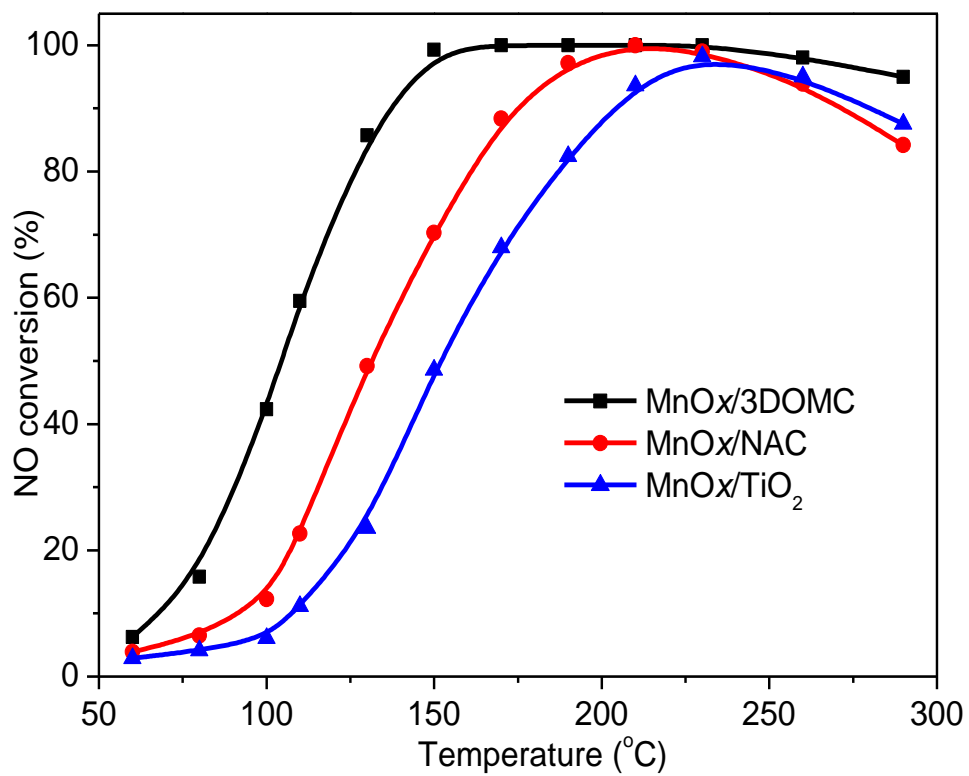


Fig. 9.

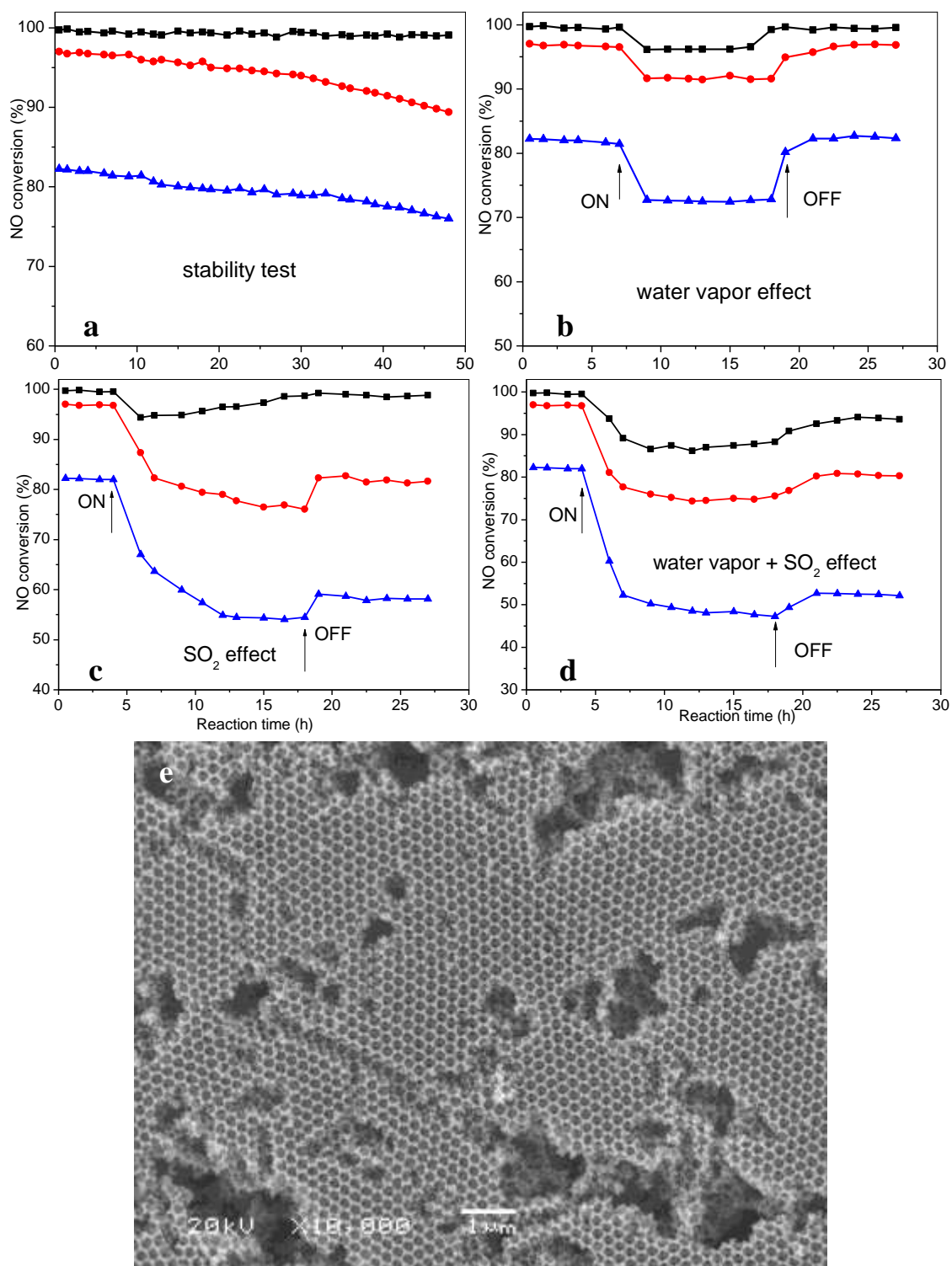


Fig. 10.

